Development of a Patient-Specific Cerebral Vasculature Fluid-Structure-Interaction Model

Kevin M. Moerman[a,**], Praneeta Konduri[b], Behrooz Fereidoonnezhad[a], Henk Marquering[b], Aad van der Lugt[c], Giulia Luraghi[d], Sara Bridio[d], Francesco Migliavacca[d], Jose F. Rodriguez Matas[d], Patrick McGarry[a,*]

[a]*National University of Ireland Galway, Galway, Ireland*
[b]*Amsterdam University Medical Centers, Amsterdam, The Netherlands*
[c]*Erasmus MC, University Medical Center, Rotterdam, The Netherlands*
[d]*Politecnico di Milano, Milano, Italy*

Abstract

Development of in silico models of patient-specific cerebral artery networks presents several significant technical challenges: (i) The resolution and smoothness of medical CT images is much lower than the required element/cell length for FEA/CFD/FSI models; (ii) contact between vessels, and indeed self contact of high tortuosity vessel segments are not clearly identifiable from medical CT images. Commercial model construction software does not provide customised solutions for such technical challenges, with the result that accurate, efficient and automated development of patient-specific models of the cerebral vessels is not facilitated. This paper presents the development of a customised and automated platform for the generation of high resolution patient-specific FEA/CFD/FSI models from clinical images. This platform is used to perform the first fluid-structure-interaction patient-specific analysis of blood flow and artery deformation of an occluded cerebral vessel. Results demonstrate that in addition to flow disruption, clot occlusion significantly alters the geometry and strain distribution in the vessel network, with the blocked M2 segment undergoing axial elongation.The new computational approach presented in this study can be further developed as a clinical

*Corresponding author
**Corresponding author
Email addresses: kevin.moerman@nuigalway.ie (Kevin M. Moerman), patrick.mcgarry@nuigalway.ie (Patrick McGarry)

diagnostic tool and as a platform for thrombectomy device design.

Keywords: Image-based modelling, Cerebral vessels, Fluid Structure Interactions, hyperelastic, non-Newtonian Flow

---

1. Introduction

Acute ischemic stroke (AIS) occurs when an intracranial artery is occluded by a thrombus, thus, decreasing the supply of blood and other nutrients to the downstream tissue. AIS is the third most frequent cause of death and the most common cause for disability among adults in Western countries [1]. The gold-standard for treatment of AIS with recombinant tissue plasminogen activator (rt-PA) and/or endovascular treatment (mechanical thrombectomy), aims to recanalize the occluded artery and restore blood supply to the affected downstream territory. Despite being effective in recanalizing the occluded artery, up to two-thirds of patients remain functionally dependent after treatment [2]. A new generation of thrombolytic drugs and mechanical intervention techniques are being developed. However, these techniques need to be tested in randomized clincial trials to be introduced in clinical practice. The INSIST consortium (IN-Silico clinical trials for treatment of acute Ischemic STroke, www.insist-h2020.eu) aims to develop an in-silico trial platform that allows for simulating randomized clinical trials to test the latest treatment developments [3].

In-silico trials is an emerging method for pre-clinical assessment of novel devices and therapeutic methods which also motivated the regulatory bodies such as US Food and Drug Administration (FDA) to develop a structured approach for assessing the credibility of computational models for medical devices [4]. Development of patient-specific finite element models from clinical images is the cornerstone of in-silico trials.

Development of in-silico models of patient-specific cerebral artery networks presents several significant technical challenges: (i) resolution and smoothness of medical CT images is much lower than the required element/cell length for FEA/CFD/FSI models; (ii) contact between vessels, and indeed self contact of high tortuosity vessel segments are not clearly identifiable from medical CT images. Commercial model construction software does not provide customised solutions for such technical challenges, with the result that accurate, efficient and automated development of patient-specific models of the cerebral vessels is not facilitated. Therefore, the main objectives of the current study are (i) to develop a customised and automated platform for the generation of high resolution patient-specific FEA/CFD/FSI models from clinical images, and (ii) to use this platform to perform the first FSI case study of blood flow and artery deformation of an occluded cerebral vessel.

2. Patient-specific model construction

In this section, segmentation and processing of medical images and the numerical method for generation of finite element meshes for artery and blood clot are described. Finite element simulation of FSI in cerebral artery is then performed using the developed patient-specific artery and blood clot meshes.

2.1. Medical image data processing and centre line construction

2.1.1. The patient data

The geometry reconstructions presented in this study are derived from clinical medical image data obtained at the Amsterdam University Medical Centers, location AMC. All data is from patients who presented with an AIS due to a large vessel occlusion in the anterior circulation, and who received endovascular treatment. The image data recorded as part of the clinical workup includes Non-Contrast Computed Tomography (NCCT) and Computed Tomography Angiography (CTA) (for more information on inclusion criteria we refer to previous work [5]). Only patient data was considered for which: 1) the NCCT image quality and resolution was was sufficient (slice thickness $\leq$2.5 mm), and 2) where the NCCT and CTA data were recorded consecutively on the same CT scanner.

2.1.2. Segmentation of the cerebral vasculature

The image-based mesh creation procedure requires a segmentation of the intracranial circulation vessel lumens from the medical image data. The term segmentation here refers to the establishment of a 3D binary image $\boldsymbol{\mathcal{S}}$ where voxel intensities are 1 on the vessel wall and inside the vessel, and 0 elsewhere.

The first step in the segmentation process is the creation of a mask which allows for the selection of the intracranial region from the CTA data. Since elements such as the skull and the carotid artery may present with similar Hounsfield Units (HUs) in the CTA data, this mask was instead derived from the NCCT data. A previously validated software featuring a threshold and region growing algorithm [6] were used for mask creation. Next, the NCCT image data was registered to the CTA data to enable mapping data from the NCCT image space to the CTA image space. This registration could be used to map the NCCT mask to create the corresponding mask for the CTA data.

Following the application of the mask, the intracranial vessels were segmented from the CTA data using custom Convolutional Neural Network (CNN) software (developed by Nico-Lab `https://www.nico-lab.com`). This

patch-based algorithm classifies voxels as vessel based on the HUs of its surrounding voxels. Since the algorithm operates in a single atlas image space the CTA data was first registered to this atlas space. Next all blood vessels could be automatically segmented using the CNN algorithm. Registration was also used to map the segmentation back to the patient CTA space.

All registrations were performed using the open source registration software Elastix [7] (version version 4.9.1, `https://elastix.lumc.nl/`).

Finally, the resulting segmentation was imported into ITK-SNAP [8] for manual processing, by a trained observer, to isolate the anterior intracranial arteries and to remove minor discrepancies in the segmentation.

Figure 1 visualises typical CTA data and a close-up of the segmentation. The segmentation offers a non-smooth voxel representation of the vascular geometry, hence further steps are required to derive smooth and high quality surface and solid meshes.

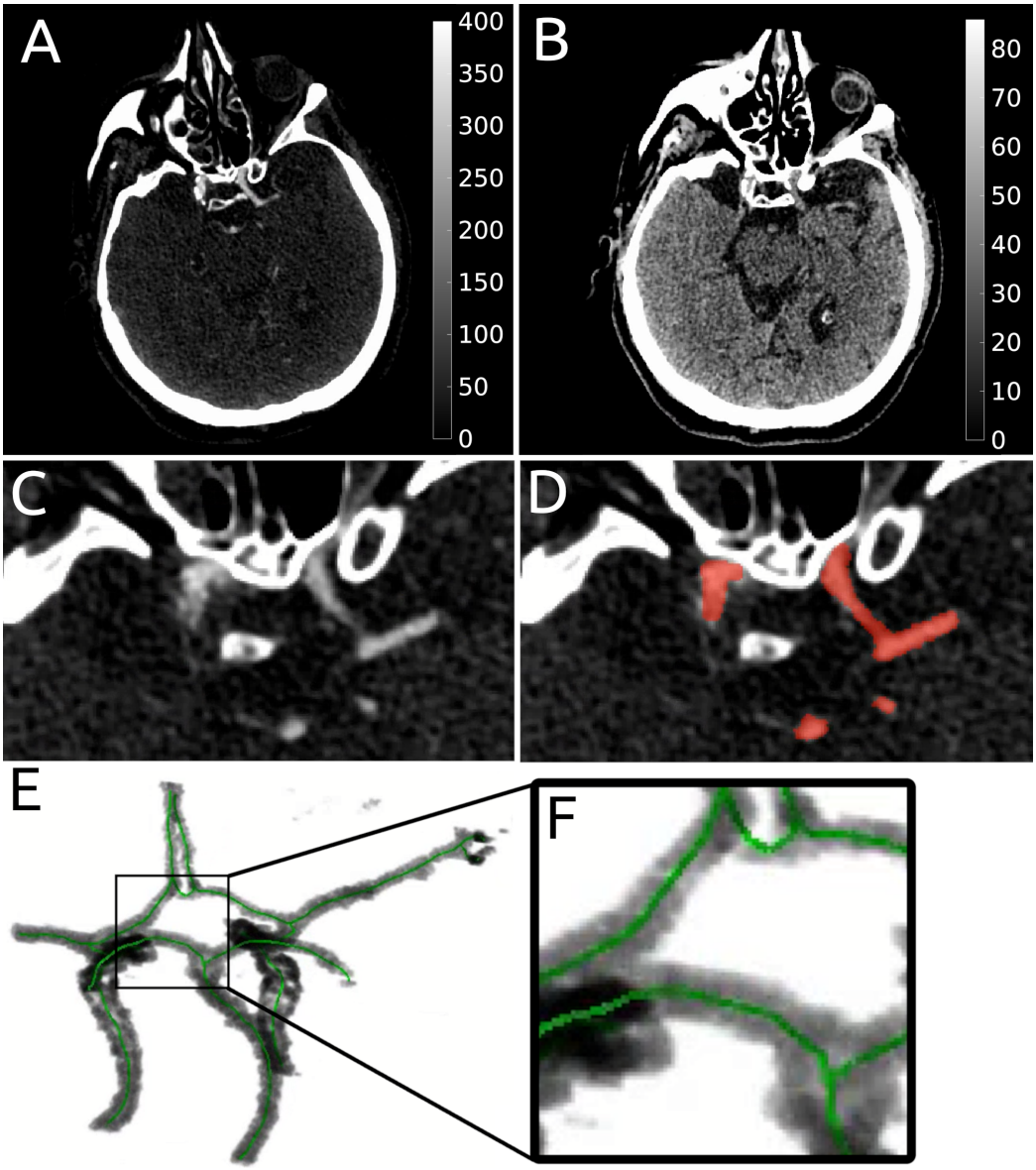

Figure 1: CTA image segmentation and centre line data construction. Axial views showing the internal carotid arteries and the basilar artery for the CTA (A), and NCCT data (B), a close-up of a CTA slice (C), a corresponding segmentation overlaid (red) (D), a shaded view of the segmentation with centre line overlaid (green) (E), and a corresponding close-up (D)

2.1.3. Vessel centre line graph construction

To aid the creation of smooth surfaces, the segmentation data is processed to provide a vessel centre line graph where information like the local radius is stored for each point on the graph. The semi-automatic software iCafe (The University of Washington, [9]) was here used to extract the center line graph, to anatomically label arterial segments, and to determine the local vessel radius at each point. The centre line and geometry measurements were also assessed by a trained observer.

The 3D coordinates for the vessel graph consists of N_G point coordinates which are arranged in a $N_G \times 3$ position vector array $\mathbf{P_G}$. Each row in $\mathbf{P_G}$ defines a position vector of a point on the graph. The local vessel radius is represented by the $N_G \times 1$ array $\mathbf{R_G}$, i.e. a single radius is defined for each graph point. Figure 2A visualizes an example of the graph, which in this case was derived from the segmentation shown in Figure 1.

The graph connectivity is defined by a set of line segments which each connect two points. The collection of all, N_E, line segments is here represented by a $N_E \times 2$ array $\mathbf{E_G}$, where all entries in the first column define indices into $\mathbf{P_G}$ of the line segment start points, while the second column defines indices into $\mathbf{P_G}$ for the line segment end points. Points in $\mathbf{P_G}$ may be shared between multiple line segments. A labelling is available for each of the N_E line segments defining the vessel type they belong to.

2.1.4. Thrombus analysis

The thrombus location and geometry characteristics were assessed by experienced neuro-radiologists using a previously presented measurement protocol [5]. In summary, the NCCT and the CTA scans were automatically registered using Elastix [7]. The hyperdense artery sign on the NCCT scans allowed the observers to select three voxels that represent the proximal, mid and distal parts of the thrombus. The length of the thrombus was measured as the distance between the proximal and distal voxels. Furthermore, in case of a bifurcating thrombus, the part of the longest part of the thrombus was assessed.

2.2. Vessel surface model construction

2.2.1. Regularization of center line data

Figure 1E and F show raw center line data plotted within the raw segmentation data. Since the raw centre line data is derived from relatively low

resolution and noisy clinical image data, the curves and radii may be non-smooth and unevenly spaced. To regularize this data the centre line data for each vessel feature were first sampled evenly (with a desired density based on the desired output finite element model mesh density). The resampling employs piecewise cubic Hermite interpolation and geodesic sampling is made possible by parameterisation based on curve length. The resampled centre line data was next smoothed (based on Humphreys-Classes smoothing [10]) in terms of the coordinates of the lines as well as data specified on the lines such as local radius. A final step in centre line regularisation is the removal of so-called vessel end artifacts. Such artifacts occur when a vessel exits the field of view of the image at an angle. The derive centre line and radii are inaccurate at these ends. All centre lines where therefore shortened by 2 mm and the radii of the last 5 mm of the ends were replaced by the radius prior to reaching the last 5 mm. An example of resampled and smoothed centre line data is shown in Figure 2A, which is the regularised version of the data in Figure 1.

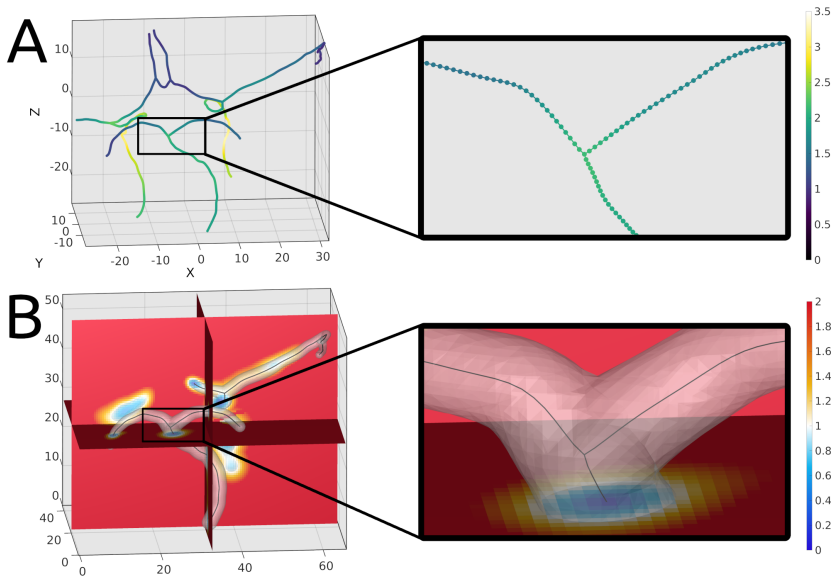

Figure 2: Processing centre lines to produces the level set image: (A) A regularised centre line, with local radii indicated by color; (B) A visualization (three mutually orthogonal slices) of the corresponding level set image with the derived vessel surface overlaid for reference.

2.2.2. Levelset image construction

The centre line data can be used for the creation of vessel surface models. Here smooth continuous surface models are constructed with the aid of level set images. level sets offer a convenient method of computing high quality surface geometry from spatial data such as the centre line graphs. Level set creation typically involves: 1) the embedding of the spatial data in an image domain, 2) defining a distance function from the spatial data to the image voxel grid, and 3) using the distance function to define a (signed) level set image. Surface geometry can then be derived through isosurface computations. See Appendix A and Figure 3 for details.

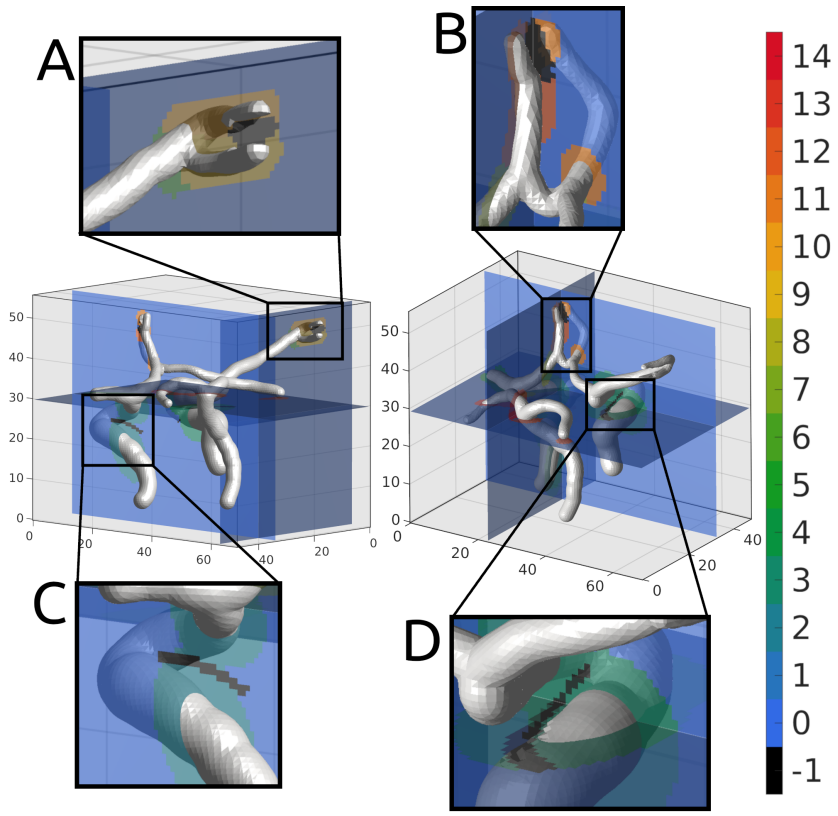

Figure 3: Visualisations (three mutually orthogonal slices) for the medial axis gradient based level set correction. Two central overview pictures and 4 close up images are provided. The derived vessel surface is overlaid for reference. The -1 intensity (black) voxels denote regions where the level set image was corrected for, 0 intensity (light blue) denotes regions outside graph neighbourhood, all other voxels are colored towards the nearest branch label. Close-ups (A) and (B) show corrections to the level set functions aiming to avoid "branch-to-branch merging". Close-ups (C) and (D) show adjustments to avoid the "self merging". Full details presented in Appendix A.

2.2.3. Triangulated surface model creation

Construction of the surface geometry is based on isosurface creation. The entire vessel surface can be retrieved from the level set image by forming the isosurface $\mathcal{L}(\mathbf{P_L}) = 1$.

Note that reconstructing surfaces at levels deviating from unity results in shrunk or expanded surfaces, e.g. iso-levels of 0.9 or 1.1 would result in a 10% decrease or increase in the resulting radii respectively.

The level set derived isosurface description contains closed vessel ends

(see also Figure 4A). For FSI simulations open inlets and outlets are required. Hence the isosurface is processed to cut open the vessel ends. The surface mesh for each vessel end was cut by a plane normal to the local graph end direction. This produced a triangulated isosurface with open ends (see also Figure 4B).

Isosurfaces typically present with a heterogeneous mesh which features many sharp and nearly collapsed triangles (see also Figure 4A and C). Therefore, the isosurfaces were remeshed to obtain a much more homogeneous and nearly-equilateral triangulation (based on a GIBBON implementation [11] of the Geogram remeshing functionality [12]). An example of remeshed surfaces is shown in Figure 4B and D.

Although the isosurface mesh spacing stems from the levelset voxel size, the remeshed mesh spacing can be chosen independently from this. Hence, one may choose a small voxel size to guaranty high fidelity of the isosurface but choose a mesh spacing during remeshing that is desired for subsequent computational analysis. In this study the mesh spacing was set at 0.5 mm (which is equivalent to the voxel size used).

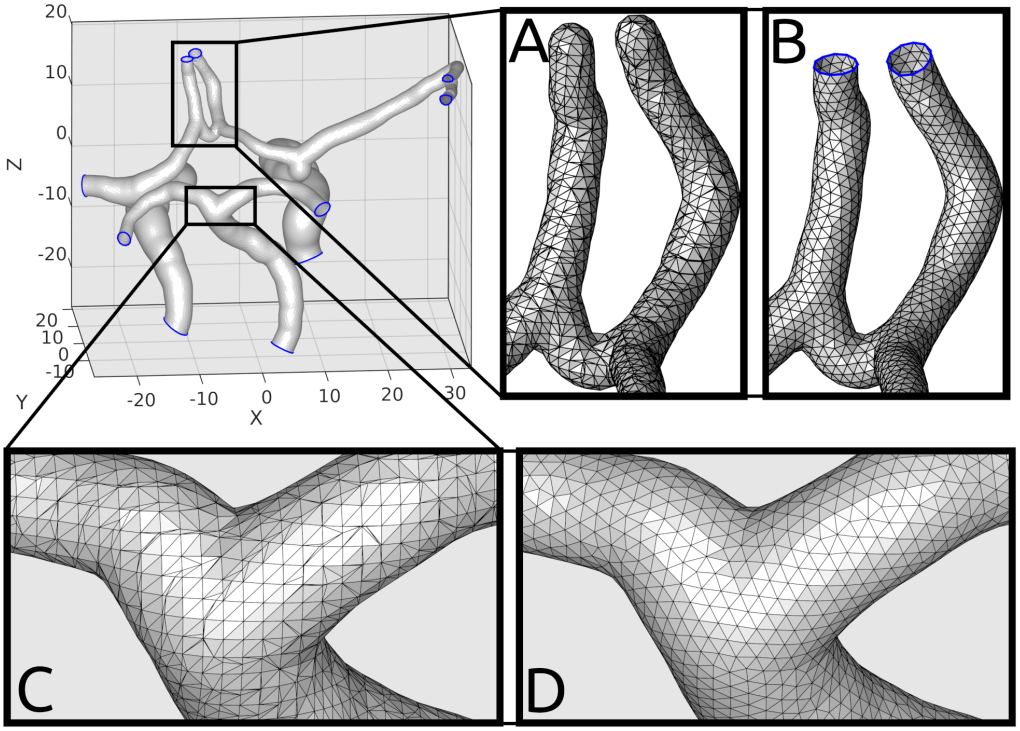

Figure 4: Processing of the isosurface to derive a high quality triangulated mesh with open vessel ends. The overview image (top left) shows the triangulated surface (gray) with vessel end boundary curves highlighted (blue). A close-up of the appearance of the rounded and closed isosurface vessel ends (A), which are cut to produce the open ends (B). A close-up (C) of the isosurface mesh, and a close-up (D) of the corresponding region showing the homogeneous near-equilateral triangulation of the final remeshed surface.

Once a triangulated surface geometry is created the fidelity with respect to the centre line data (i.e. the radii) can be verified. For each node on the mesh the nearest center line graph point can be computed. Furthermore, the radius at each graph point can be compared to the distance of the graph point to the mesh node. In figure 5A an example mesh is shaped towards the difference between the radius implied by the nearest graph point and the perceived mesh radius (shortest distance from mesh to graph). Figure 5B shows a histogram for the differences across the entire mesh. This example mesh presented with a near-zero mean difference ($8.65 \cdot 10^{-4}$ mm), and a standard deviation of 0.0310 mm.

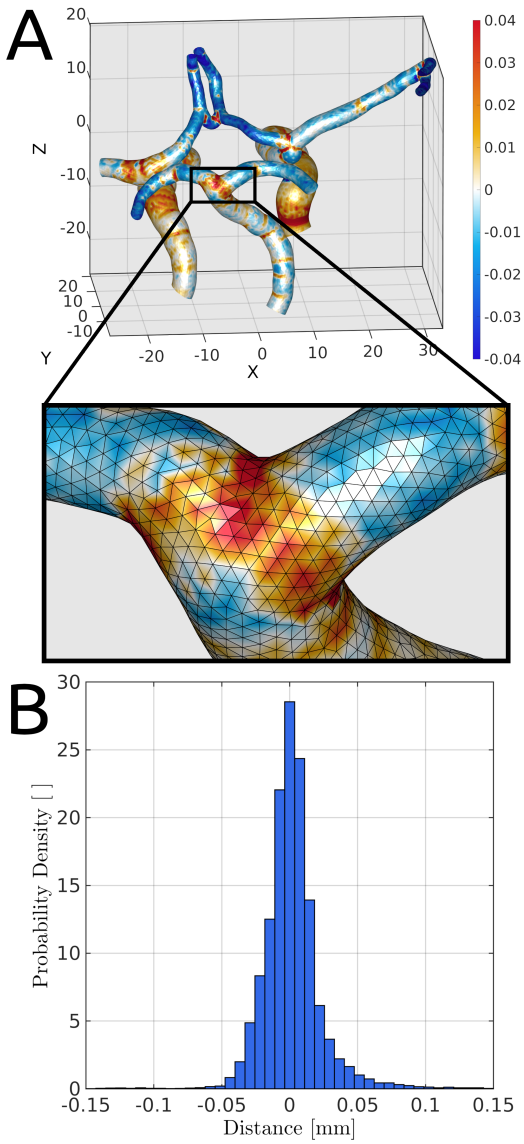

Figure 5: The surface deviation with respect to the center line graph radius data.

It should be noted that the accuracy of the surface reconstructions heavily depends on the chosen voxel size, and the remeshing point spacing (both 0.5 mm in this example). Lower errors can be achieved if these control parameters are decreased (although at the cost of increased computational time). In this study, with the parameters mentioned, the computational time for

the creation of a single surface mesh (from raw centre line data to the final remeshed triangulated surface and difference evaluation) is approximately 13 seconds (on a laptop featuring 32Gb RAM and an 4 core 2.90 GHz CPU). Since this process is automated it can easily be applied for high-throughput applications. To demonstrate this capability, figure 6 illustrates the application of the presented methods for N=50 patient-specific data sets, which took under 11 minutes to complete.

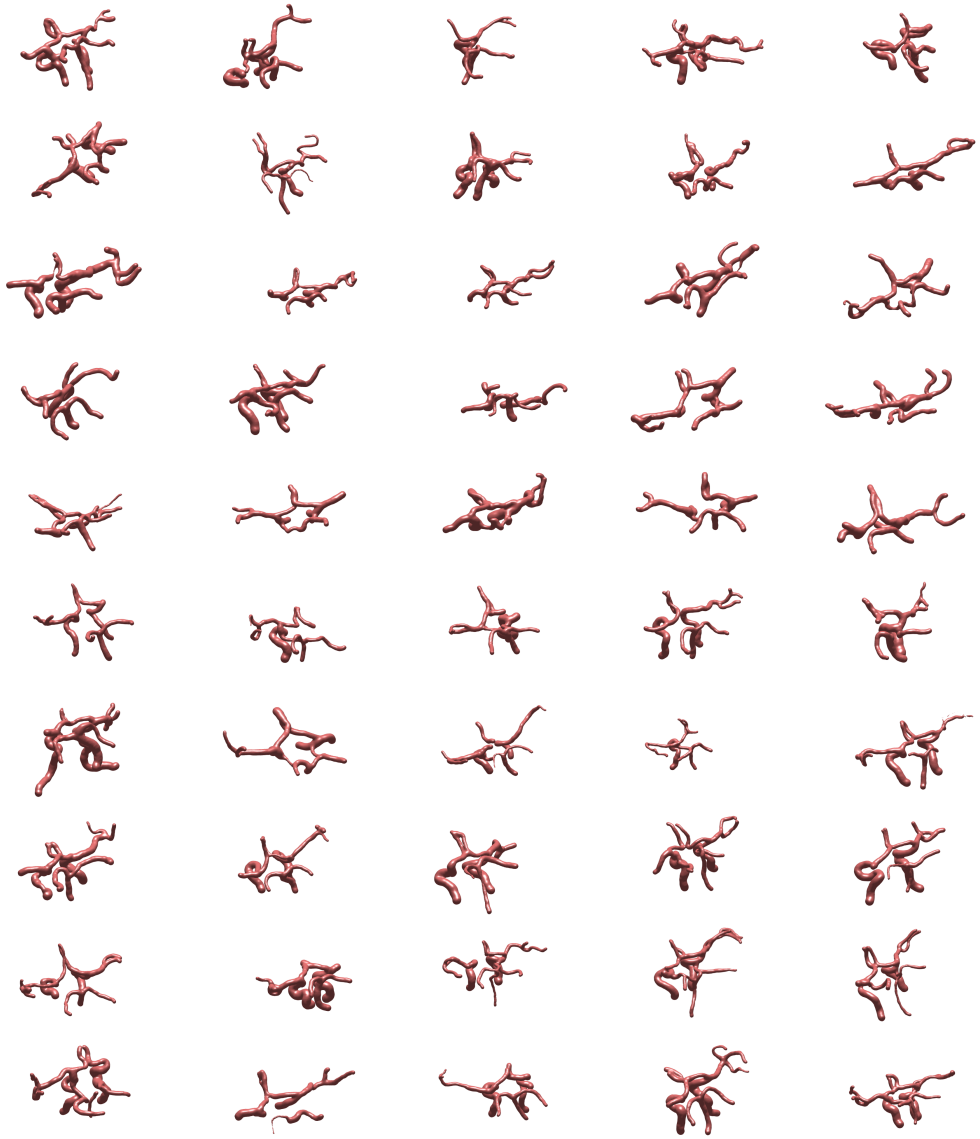

Figure 6: Triangulated surface models of intracranial vessel trees.

2.3. Clot surface model creation

The thrombus location information, described in section 2.1.4, can be mapped to the centre line graph. Using a nearest point mapping between the mesh and the graph, the mapping can be translated to the vessel surface

mesh. The clot location can therefore literally be painted on the vessel surface. Figure 7 illustrates how a clot mesh can be automatically created by locally cloning the vessel mesh to form the clot body, and by closing over this cloned section by smooth end caps (based on the GIBBON *regionTriMesh3D* function).

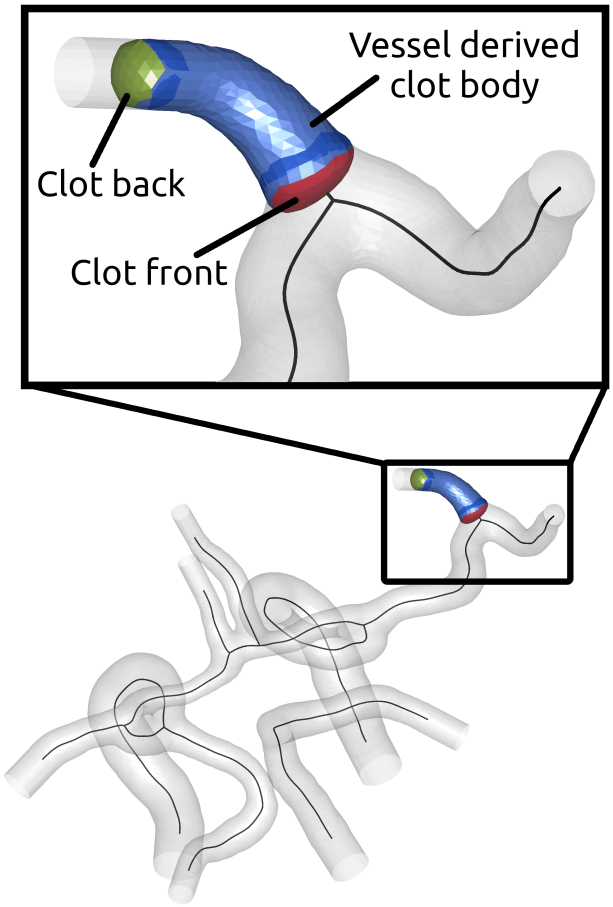

Figure 7: Illustration of clot meshing by cloning the local vessel to create the clot body, and by closing the clot ends using a smooth cap.

2.4. Solid meshing

If, rather than a surface mesh, solid elements are required for the vessel wall, these can be created through thickening of the mesh. The thickening can be based on a constant or a spatially varying wall thickness, e.g. as provided

along the center line. Thickening of a triangulated mesh creates layers of pentahedral (or wedge) elements (or hexahedral elements if the triangulation is first converted to a quadrangulation). The interior of the clot is here meshed using tetrahedral elements (using the GIBBON implementation of TetGen [13]).

3. Patient-specific FSI simulation

To demonstrate the advanced capabilities of the framework an FSI case study is presented using the highlighted patient-specific mesh in Figure 7. All FEA and FSI simulations are conducted using the open source software FEBio (v1.9.1 `https://febio.org/` [14]). The recently added FSI capabilities are detailed in Ateshian et al. [15] and Shim et al. [16].

3.1. Automated FSI model creation

Figure 8A shows the curved anatomy of a patient-specific vessel (corresponding to the 4th row, 2nd column in 6) with an extended straight section towards the left. A gradient of vessel wall stiffness is specified along the extended straight section. From the start of the inlet to the region of interest, as illustrated in Figure 8B, the stiffness alters from 20 times the normal stiffness to a physiological value at the start of the region of interest. This causes the vessel wall to remain relatively undeformed at the inlet while reaching the correct level of deformation at the intersection of the straight section and the patient-specific vessel. The addition of the straight section is necessary to achieve fully developed flow profiles at the start of the patient-specific vessels in the region of interest, and to ensure that any artificially high strain concentrations in the vessel wall near the inlet do not impact on results in the region of interest. Other boundary conditions are highlighted in Figure 8C, D: the vessel and fluid ends are fully constrained in terms of displacement, and the inner vessel wall has no-slip boundary conditions. Details of the mesh for the vessel wall, clot and fluid domain are shown in Figure 8E, F, with extruded pentahedral elements in the vessel wall (thickness 0.3 mm) and tetrahedral elements for the clot and the fluid domain. The entire model creation process, from patient-specific mesh creation to boundary condition configuration, as well as the simulation execution procedure, were automated by coding the process in GIBBON [11].

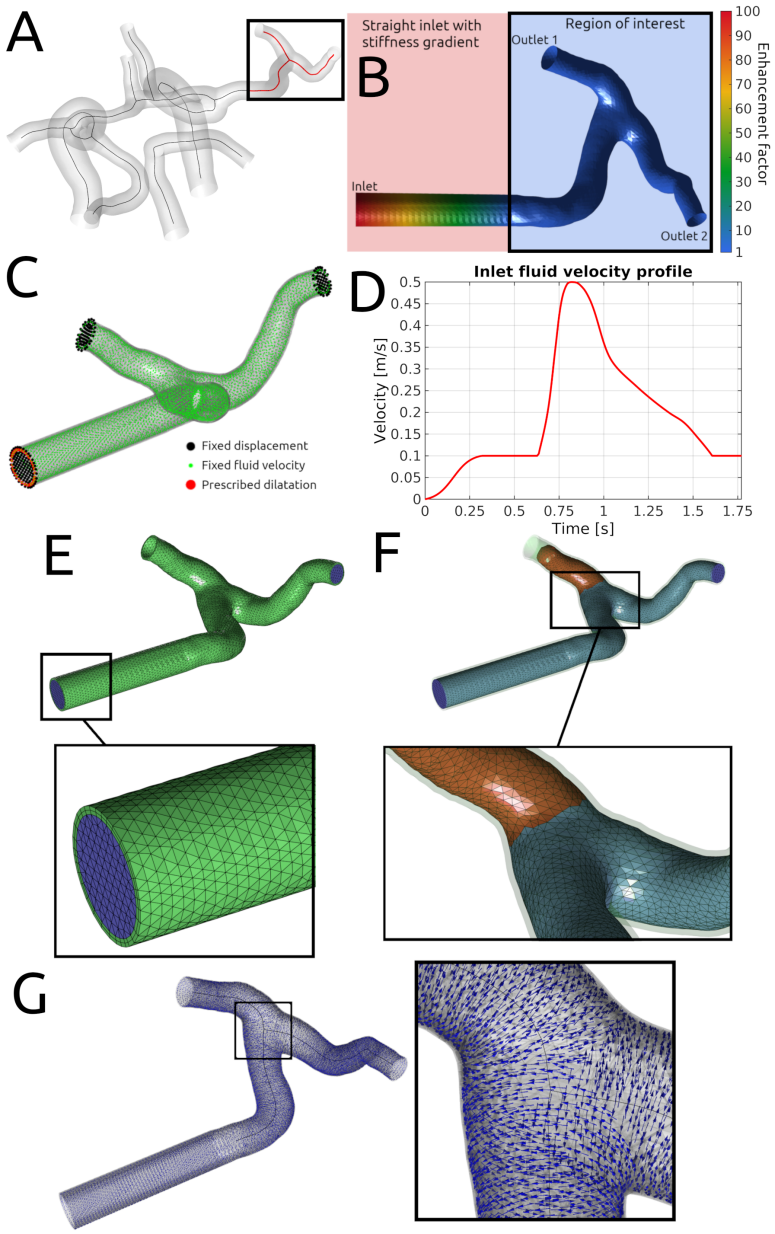

Figure 8: FSI model configuration. The M1-M2 segment of a vascular tree (A) is used to build a model with an extended straight section (shaded towards stiffness enhancement factor) (B). Boundary conditions are visualised in (C) and the inlet velocity profile conditions is shown (D). Visualisations for the pentahedral vessel (green) (E) and tetrahedral fluid (blue) and clot (red) (F) mesh domains are shown. An example of the mapping of local (circumferential) fibre directions (G).

The velocity at the inlet surface is prescribed using reported velocity measurements in cranial vessels [17], as shown in Figure 8D. The total fluid pressure at the outlets is given as $P_{tot} = P_0 + P_h = RF$, where R is the specified value of peripheral resistance ($4 \times 10^8\ Pa \cdot m^{-1} \cdot s$), P_0 is a specified baseline pressure [16], F is the computed volumetric flow, and P_h is the computed haemodynamic pressure. At the start of the simulation the baseline velocity and the baseline pressure P_0 are smoothly increased to the specified value such that fully developed steady state flow is computed. Following this initial step, 3 cardiac cycles are simulated.

Non-Newtonian behaviour of blood is modelled using the Carreau model [18], for which the viscous shear stress $\boldsymbol{\tau}$ is given by:

$$\boldsymbol{\tau} = 2\mu\mathbf{D} \tag{1}$$

where

$$\mu = \mu_\infty + (\mu_0 + \mu_\infty)(1 + (\lambda\dot{\gamma})^2)^{\frac{n-1}{2}} \tag{2}$$

in which $\mu_0 = 0.056\ Pa \cdot s$ is the shear viscosity at the zero shear rate, $\mu_\infty = 0.00345\ Pa \cdot s$ is the shear viscosity at the infinite shear rate, $\lambda = 3.313$ s is a time constant, $n = 0.3658$ is a power-law exponent, and $\dot{\gamma} = \sqrt{2\mathbf{D} : \mathbf{D}}$ is the engineering shear rate. The density for blood was set at 1060 kg/m^3. All blood parameters are from [18] (as also used in [16]).

The constitutive behaviour of the clot and the vessel wall is modelled using the following Ogden hyperelastic formulation [19]:

$$\Psi_{iso}(\lambda_1, \lambda_2, \lambda_3) = \frac{\kappa}{2}(J-1)^2 + \sum_{i=1}^{N} \frac{c_i}{{m_i}^2}\left({\lambda_1}^{m_i} + {\lambda_2}^{m_i} + {\lambda_3}^{m_i} - 3 - m_i \ln(J)\right) \tag{3}$$

where Ψ represents the strain energy density, λ_i are the principal stretches, c_i represent shear-modulus-like material parameters, m_i are parameters controlling the degree of non-linearity, and κ represents a bulk-modulus-like material parameter. The parameter N sets the model order. Motivated by Moerman et al. [20] we use $N = 2$, $c = c_1 = c_2$, $m = m_1 = -m_2$ for both the clot and the vessel.

Moreover, the anisotropy of vessel wall is incorporated by adding the contribution of collagen fibres strain energy to the Ogden formulation for non-collagenous matrix (equation 3); i.e., $\Psi = \Psi_{iso} + \Psi_f$. The following

form of strain energy density function is used for collagen fibres (FEBio [14] *Fiber with Exponential-Power Law*):

$$\Psi_f(\lambda_F) = \frac{\xi}{\alpha\beta}\left(\exp\left(\alpha(\lambda_F^2 - 1)^\beta\right) - 1\right) \tag{4}$$

where $\xi > 0$ is the fibre modulus, $\alpha > 0$ and $\beta \leq 2$ control the strain stiffening behaviour of the fibre, and λ_F is the stretch along the fibre. Here $\beta = 2$ is used. The collagen fibres in each element are in the local circumferential axial plane (see Figure 8G). To calculate the local coordinates of each element, the nearest centre line direction vector is computed which provides the local axial direction. The cross product between the axial vector and the vector pointing from the element to the nearest centre line point (radial direction) is then the circumferential direction. Fibres can be defined in the circumferential direction (see Figure 8G) or rotated around the axial direction by an angle θ (e.g. $\theta = 0°$ indicates circumferential fibres and $\theta = 90°$ indicates axial fibres).

Vessel material parameters are calibrated using published experimental stress-strain relationships for cranial vessels [21], resulting in the following material parameters: $c = 0.2$ MPa, $m = 2$, $\xi = 25$ kPa, $\alpha = 2$, and $\beta = 2$ (note that if $J \approx 1$ the use of $m = 2$ reduces the model to a Mooney-Rivlin formulation). The density for the vessel wall was set at 1000 kg/m^3 [16].

The clot material properties are calibrated using experimental data from unconfined compression tests on clot analogues [22], resulting in the following material parameters: $c = 0.2$ MPa; $m = 2$. The clot material density was set at 1000 kg/m^3. Near incompressible (volume preserving) behaviour is enforced for the clot and vessel by setting $\kappa = 500 \cdot c$.

It should be noted that the objective of the FSI simulation in this study is to demonstrate the capability of the developed platform and therefore these basic material models and parameters for the clot and artery are considered sufficient. More sophisticated material models such as those recently proposed for blood clots [23, 24] and vessel walls [25] should be considered in future studies.

3.2. FSI Results

A parametric study has been performed to parse the influence of vessel and flow properties on the results (Table 1) in a non-occluded patient-specific artery. Results of this parametric study are presented in Table 2 in terms of the following computed quantities: (i) peak vessel wall strain at bifurcation

at peak systole; (ii) Mean strain in patient-specific vessels at peak systole; (iii) Mean strain in patient-specific vessels at diastole; (iv) peak velocity at Outlet 1 and Outlet 2. Computed strains are expressed as the Von Mises strain. Simulations reveal that circumferentially orientated fibres in the vessel wall (Model 1) result in lower wall strains than those computed for axial fibres (Model 2). In fact, the mean vessel wall strains are similar for axial fibres (Model 2) and an isotropic vessel wall without fibres (Model 3). These results are expected, given that vessel strains are primarily circumferential direction due to lumen pressure loading. Neither the vessel anisotropy nor the specified baseline pressure P_o has a strong influence on computed flow velocity at the vessel outlets. An increased peak systole velocity at the inlet (Model 6) results in an increase in mean vessel wall strain and outlet velocity during systole.

Figure 9 shows the computed strain state in the M1, M2 Superior Trunk and M2 Inferior Trunk branches of a vessel in the absence of a clot occlusion. The principal strain direction is largely in the circumferential direction, and the effective strain is highest in the bifurcation region. Table 2 presents influence of vessel wall fibre orientation, outlet pressure, and input velocity on vessel wall strain and blood flow. Circumstantially orientated fibres result in a reduced vessel wall strain. As expected, an increase in outlet pressure increases vessel wall strain. Outlet velocities are not strongly influenced by the orientation of vessel wall fibres. An increase of inlet velocity leads to an increase in vessel wall strain and outlet velocity, as expected.

Table 1: Model input parameter values.

Model	Description	Vessel Wall Properties	Peak inlet velocity (m/s)	P_0 (Pa) at Outlets 1 and 2
1	Circumferential Fibres	c=0.2 MPa, $\xi = 25$ kPa, $\theta = 0^o$	0.5	1.0e4
2	Axial fibres	c=0.2 MPa, $\xi = 25$ kPa, $\theta = 90^o$	0.5	1.0e4
3	Isotropic (no fibres)	c=0.2 MPa, $\xi = 0$ kPa, θ =N/A	0.5	1.0e4
4	Increased Pressure	c=0.2 MPa, $\xi = 25$ kPa, $\theta = 0^o$	0.5	1.2e4
5	Reduced Pressure	c=0.2 MPa, $\xi = 25$ kPa, $\theta = 0^o$	0.5	0.8e4
6	Increased inlet velocity	c=0.2 MPa, $\xi = 25$ kPa, $\theta = 0^o$	0.6	1.0e4
7	Reduced inlet velocity	c=0.2 MPa, $\xi = 25$ kPa, $\theta = 0^o$	0.4	1.0e4

Table 2: Effect of anisotropy, pressure, and fluid velocity

Model	Peak strain at bifurcation	Mean strain at systole	Mean strain at diastole	Peak velocity inlet 1 (m/s)	Peak velocity inlet 2 (m/s)
1	0.32	0.155	0.132	1.020	1.231
2	0.39	0.187	0.156	1.002	1.230
3	0.59	0.187	0.156	1.003	1.229
4	0.46	0.188	0.163	0.998	1.114
5	0.33	0.126	0.103	1.042	1.139
6	0.41	0.162	0.132	1.198	1.345
7	0.38	0.149	0.132	0.832	0.919

Computed streamlines are compared for a clot occluded vessel and an non-occluded vessel in Figure 10. The blocking of the M2 Superior Trunk vessel results in increased flow velocity throughout the M1 and M2 Inferior Trunk branches. Importantly, network geometry is dramatically altered by the altered flow patterns. The spatial position of the bifurcation is altered by 4 mm due to the flow disruption. As shown in Figure 11, the M2 Superior Trunk vessel elongates, undergoing a state of tension. the direction of principal strain in the M2 Superior Trunk branch is primarily in the axial direction, rather than the circumferential direction for the non-occluded vessel, again highlighting the increased axial tension in the M2 Superior Trunk vessel. Finally, the effective strain in the clot is significantly higher proximally, and reduces towards the distal end of the clot (Figure 11E, F).

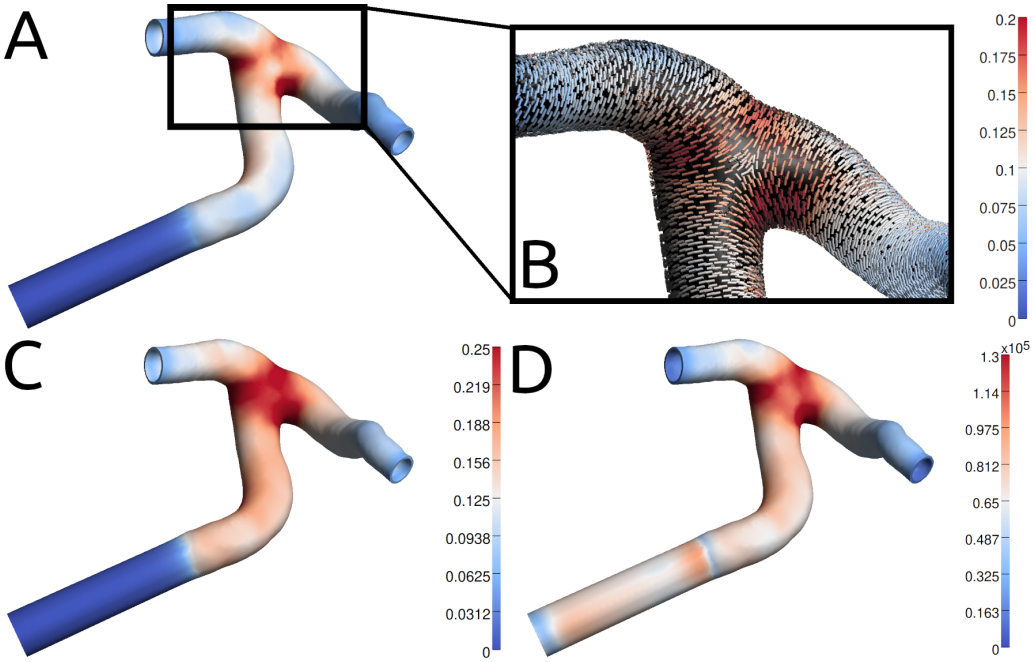

Figure 9: FSI simulation results at peak input velocity for the circumferentially orientated fibre model (Model 1). The first principal (Green-Lagrange) strains (A), and a close-up of their directions (B). The effective (Green-Lagrange) strain (C), and the Von Mises stress (Pa) (D), and a vector (E) and stream-line plot for the relative flow velocity (m/s).

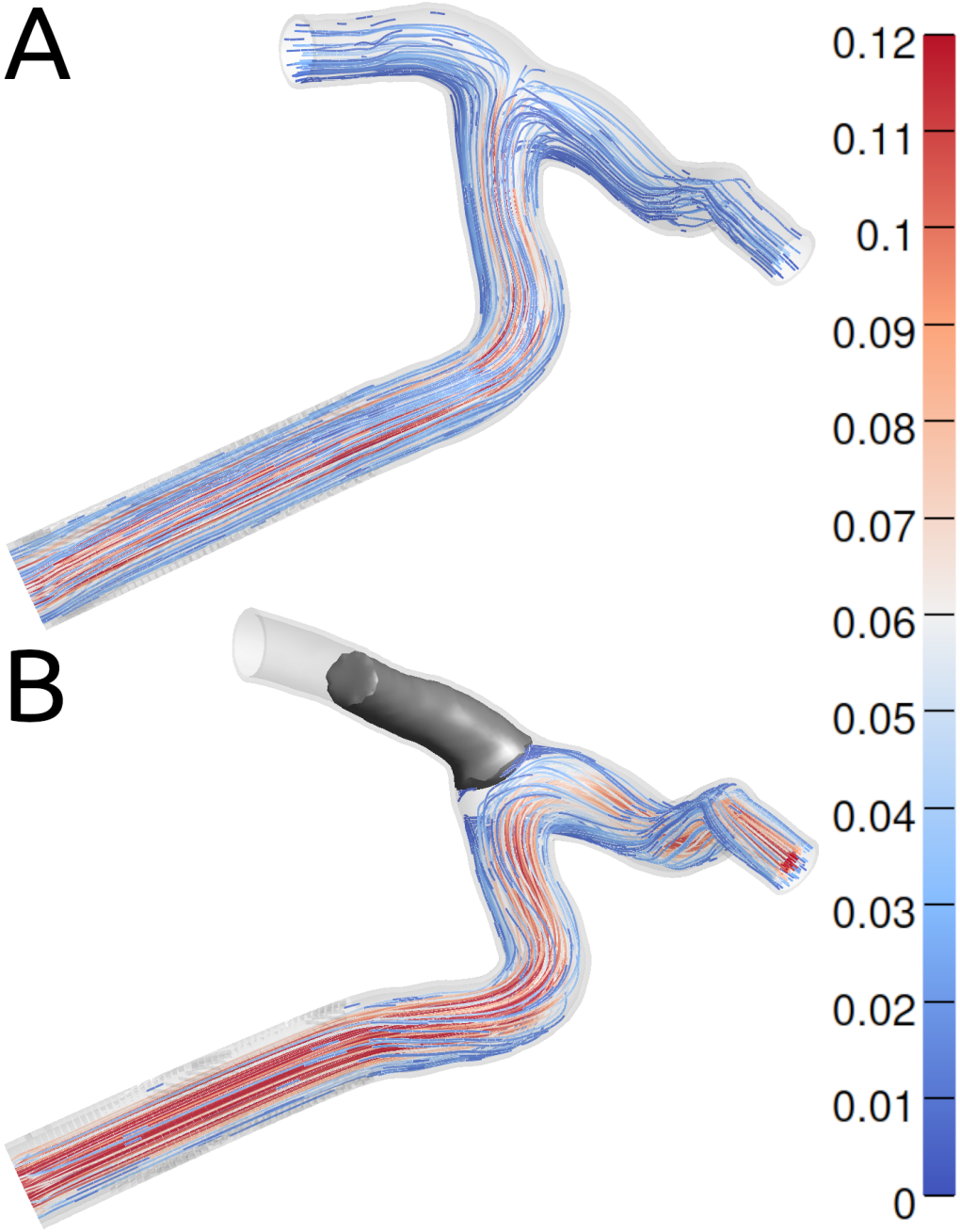

Figure 10: Stream-line visualisations of the relative flow velocity (m/s) for the FSI simulations at peak input velocity for the circumferentially orientated fibre model (Model 1). A model configuration without a clot (A) and with a clot (shown in solid gray) (B).

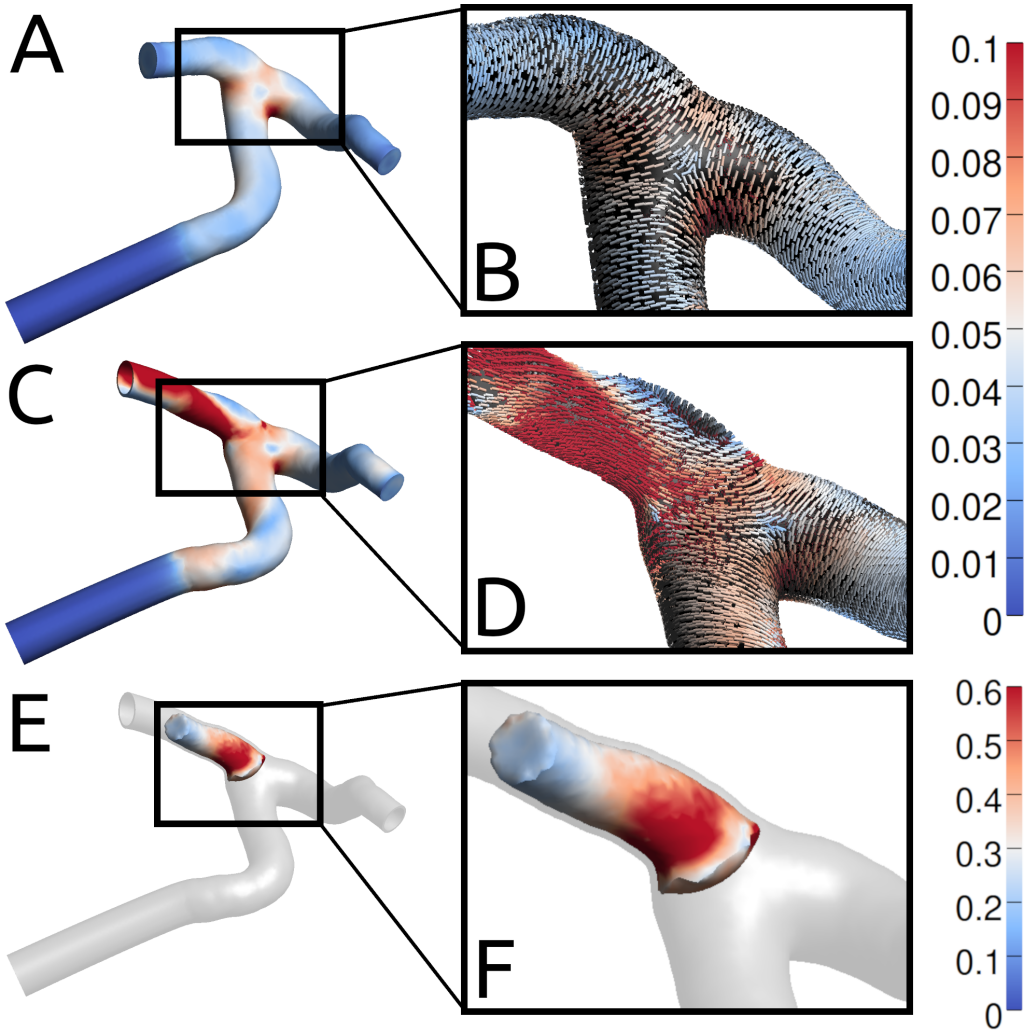

Figure 11: The first principal strain for the vessel without the clot (A), and a close-up of their directions (B), the corresponding data for the vessel with a clot (C), and a close-up of their directions (D). The effective strain in the clot (E), and a close up (F)

4. Concluding remarks

A novel numerical methodology has been developed to create meshes of the brain vasculature based on medical image data. The medical image data is processed to provide vessel centre line and radius information. Surface or solid meshes are next derived from level set images computed from these centre line descriptions. The developed numerical methodology provides a

platform for generating fully automated patient-specific finite element models from medical images which serves as the cornerstone of in-silico models. The suitability of the meshes for computational analysis is demonstrated for solid mechanics and fluid-structure interaction simulations. Moreover, a parameter study was performed to parse the effect of vessel wall mechanical properties, fluid flow at the inlet boundary and prescribed fluid pressure at the outlet boundary on the stress and strain in the vessel wall and blood velocity at the outlet of the region of interest. Moreover, the developed finite element model has been used for finite element simulation of the first patient-specific thrombectomy procedure and the results have been presented in a follow-on submitted study [26].

5. Acknowledgements

This project was funded by a European Union Horizon 2020 Research and Innovation Program, under grant agreement No. 777072. The authors are grateful to Dr Jay Shim and Prof Gerard Ateshian (Columbia University, New York, USA) for providing advice on the FEBio FSI implementation.

[1] G. . Mortality, C. of Death Collaborators, Global, regional, and national agesex specific all-cause and cause-specific mortality for 240 causes of death, 19902013: a systematic analysis for the Global Burden of Disease Study 2013, The Lancet 385 (2015) 117–171.

[2] O. A. Berkhemer, P. S. Fransen, D. Beumer, L. A. van den Berg, H. F. Lingsma, A. J. Yoo, W. J. Schonewille, J. A. Vos, P. J. Nederkoorn, M. J. Wermer, M. A. van Walderveen, J. Staals, J. Hofmeijer, J. A. van Oostayen, G. J. Lycklama Nijeholt, J. Boiten, P. A. Brouwer, B. J. Emmer, S. F. de Bruijn, L. C. van Dijk, L. J. Kappelle, R. H. Lo, E. J. van Dijk, J. de Vries, P. L. de Kort, W. J. J. van Rooij, J. S. van den Berg, B. A. van Hasselt, L. A. Aerden, R. J. Dallinga, M. C. Visser, J. C. Bot, P. C. Vroomen, O. Eshghi, T. H. Schreuder, R. J. Heijboer, K. Keizer, A. V. Tielbeek, H. M. den Hertog, D. G. Gerrits, R. M. van den Berg-Vos, G. B. Karas, E. W. Steyerberg, H. Z. Flach, H. A. Marquering, M. E. Sprengers, S. F. Jenniskens, L. F. Beenen, R. van den Berg, P. J. Koudstaal, W. H. van Zwam, Y. B. Roos, A. van der Lugt, R. J. van Oostenbrugge, C. B. Majoie, D. W. Dippel, A Randomized Trial of Intraarterial Treatment for Acute Ischemic Stroke, New England Journal of Medicine 372 (2015) 11–20.

[3] P. R. Konduri, H. A. Marquering, E. E. van Bavel, A. Hoekstra, C. B. L. M. Majoie, T. I. Investigators, In-Silico Trials for Treatment of Acute Ischemic Stroke, Frontiers in Neurology 11 (2020).

[4] V V 40 ASME Standard, Assessing credibility of computational modeling through verification and validation: Application to medical devices, 2018.

[5] Dutra Bruna G., Tolhuisen Manon L., Alves Heitor C.B.R., Treurniet Kilian M., Kappelhof Manon, Yoo Albert J., Jansen Ivo G.H., Dippel Diederik W.J., van Zwam Wim H., van Oostenbrugge Robert J., da Rocha Antnio J., Lingsma Hester F., van der Lugt Aad, Roos Yvo B.W.E.M., Marquering Henk A., Majoie Charles B.L.M., null null, Thrombus Imaging Characteristics and Outcomes in Acute Ischemic Stroke Patients Undergoing Endovascular Treatment, Stroke 50 (2019) 2057–2064.

[6] R. S. Barros, M. L. Tolhuisen, A. M. Boers, I. Jansen, E. Ponomareva, D. W. J. Dippel, A. v. d. Lugt, R. J. v. Oostenbrugge, W. H. v. Zwam,

O. A. Berkhemer, M. Goyal, A. M. Demchuk, B. K. Menon, P. Mitchell, M. D. Hill, T. G. Jovin, A. Davalos, B. C. V. Campbell, J. L. Saver, Y. B. W. E. M. Roos, K. W. Muir, P. White, S. Bracard, F. Guillemin, S. D. Olabarriaga, C. B. L. M. Majoie, H. A. Marquering, Automatic segmentation of cerebral infarcts in follow-up computed tomography images with convolutional neural networks, Journal of NeuroInterventional Surgery 12 (2020) 848–852.

[7] S. Klein, M. Staring, K. Murphy, M. A. Viergever, J. P. W. Pluim, elastix: A Toolbox for Intensity-Based Medical Image Registration, IEEE Transactions on Medical Imaging 29 (2010) 196–205.

[8] P. A. Yushkevich, J. Piven, H. C. Hazlett, R. G. Smith, S. Ho, J. C. Gee, G. Gerig, User-guided 3D active contour segmentation of anatomical structures: Significantly improved efficiency and reliability, NeuroImage 31 (2006) 1116–1128.

[9] L. Chen, M. Mossa-Basha, N. Balu, G. Canton, J. Sun, K. Pimentel, T. S. Hatsukami, J.-N. Hwang, C. Yuan, Development of a quantitative intracranial vascular features extraction tool on 3d MRA using semiautomated open-curve active contour vessel tracing, Magnetic Resonance in Medicine 79 (2018) 3229–3238.

[10] J. Vollmer, R. Mencl, H. Mller, Improved Laplacian Smoothing of Noisy Surface Meshes, Computer Graphics Forum 18 (1999) 131–138.

[11] K. M. Moerman, GIBBON: The Geometry and Image-Based Bioengineering add-On, The Journal of Open Source Software 3 (2018) 506.

[12] B. Levy, N. Bonneel, Variational Anisotropic Surface Meshing with Voronoi Parallel Linear Enumeration, in: X. Jiao, J.-C. Weill (Eds.), Proceedings of the 21st International Meshing Roundtable, Berlin, Heidelberg, pp. 349–366.

[13] H. Si, TetGen, a Delaunay-Based Quality Tetrahedral Mesh Generator, ACM Transactions on Mathematical Software 41 (2015) 1–36.

[14] S. A. Maas, B. J. Ellis, G. A. Ateshian, J. A. Weiss, FEBio: Finite Elements for Biomechanics, Journal of Biomechanical Engineering 134 (2012) 011005.

[15] G. A. Ateshian, J. J. Shim, S. A. Maas, J. A. Weiss, Finite element framework for computational fluid dynamics in FEBio, Journal of Biomechanical Engineering 140 (2018).

[16] J. J. Shim, S. A. Maas, J. A. Weiss, G. A. Ateshian, A Formulation for FluidStructure Interactions in febio Using Mixture Theory, Journal of Biomechanical Engineering 141 (2019) 051010–15.

[17] B. M. W. Cornelissen, J. J. Schneiders, M. E. Sprengers, R. v. d. Berg, P. v. Ooij, A. J. Nederveen, E. v. Bavel, W. P. Vandertop, C. H. Slump, H. A. Marquering, C. B. L. M. Majoie, Aneurysmal Parent ArterySpecific Inflow Conditions for Complete and Incomplete Circle of Willis Configurations, American Journal of Neuroradiology 39 (2018) 910–915.

[18] Y. I. Cho, K. R. Kensey, Effects of the non-Newtonian viscosity of blood on flows in a diseased arterial vessel. Part 1: Steady flows, Biorheology 28 (1991) 241–262.

[19] R. Ogden, Non-linear elastic deformations, Dover Publications Inc., Mineola, New York, 1984.

[20] K. M. Moerman, C. K. Simms, T. Nagel, Control of tension-compression asymmetry in Ogden hyperelasticity with application to soft tissue modelling, Journal of the Mechanical Behavior of Biomedical Materials 56 (2016) 218–228.

[21] K. L. Monson, N. M. Barbaro, G. T. Manley, Biaxial response of passive human cerebral arteries, Annals of Biomedical Engineering 36 (2008) 2028–2041.

[22] S. Johnson, R. McCarthy, M. Gilvarry, P. E. McHugh, J. P. McGarry, Investigating the mechanical behavior of clot analogues through experimental and computational analysis, Annals of Biomedical Engineering 49 (2021) 420–431.

[23] B. Fereidoonnezhad, K. M. Moerman, P. McGarry, A new hyperelastic model for the multi-axial deformation of blood clots occlusion in vessels, Biomechanics and Modeling in Mechanobiology (2020) , in press.

[24] B. Fereidoonnezhad, A. Dwivedi, S. Johnson, R. McCarthy, P. McGarry, Blood clot fracture properties are dependent on red blood cell and fibrin content, bioRxiv (2020).

[25] B. Fereidoonnezhad, C. OConnor, J. McGarry, A new anisotropic soft tissue model for elimination of unphysical auxetic behaviour, Journal of Biomechanics 111 (2020) 110006.

[26] G. Luraghi, S. Bridio, J. F. Rodriguez Matas, G. Dubini, N. Boodt, F. J. H. Gijsen, A. van der Lugt, B. Fereidoonnezhad, K. Moerman, P. McGarry, P. Konduri, N. A. Terreros, H. A. Marquering, C. B. Majoie, F. Migliavacca, The first virtual patient-specific thrombectomy procedure, Journal of Biomechanics (2021) , under review.

Appendix A. Levelset image construction

A 3D level set image matrix $\boldsymbol{\mathcal{L}}(\mathbf{P_L})$ is defined, in which the feature is embedded, consisting of N_L voxels. A desired voxel size can be set which controls the point spacing used for the reconstruction of an isosurface defining the vessel geometry. In this study a voxel size of 0.5 mm is used.

The following Euclidian distance matrix $\mathbf{D}(\mathbf{P_G}, \mathbf{P_L})$ is computed:

$$D_{ij} = \sqrt{\sum_{k=1}^{3} (P_{Gik} - P_{Ljk})^2} \tag{A.1}$$

Here i ($i \in [1, N_G]$) is the row index for $\mathbf{P_G}$ and j ($j \in [1, N_L]$) is the row index for the level set image voxel coordinate array $\mathbf{P_L}$. The index k is for the x, y, and z coordinates.

Note that a full distance computation (requiring a $N_L \times N_G$ array) is omitted here for computational efficiency. Instead the numerical implementation features distance computation only for voxels within the so-called graph neighbourhood (up to twice the vessel radius removed from $\mathbf{P_G}$). Identification of this subset is here based on a mask derived from the dilation of a binary "graph image" $\boldsymbol{\mathcal{S}_G}$ (the indices of "true" voxels are found from spatial-to-image coordinate conversion of $\mathbf{P_G}$) (alternatively a resampled and dilated version of the segmentation image $\boldsymbol{\mathcal{S}}$ can be used).

Finally the level set image $\boldsymbol{\mathcal{L}}(\mathbf{P_L})$ is defined as:

$$\mathcal{L}_{\alpha\beta\gamma} = \mathcal{L}_j = \min^{(i)} \left(\frac{D_{ij}}{R_{Gi}} \right) \tag{A.2}$$

Here α, β, γ are the row, column, and slice indices of the level set image $\boldsymbol{\mathcal{L}}(\mathbf{P_L})$. The index j is the previously defined row index of $\mathbf{P_L}$ or equivalently the linear voxel index (or voxel number) for $\boldsymbol{\mathcal{L}}(\mathbf{P_L})$ (i.e. $j = \alpha\beta\gamma$). The operator $\min^{(i)}$ stands for the minimum along the i, or row, index direction.

With the above definition the level set image has the following properties:

$$\begin{cases} \mathcal{L}(\mathbf{P_L}) = 0 & \text{Vessel centre} \\ \mathcal{L}(\mathbf{P_L}) < 1 & \text{Vessel interior} \\ \mathcal{L}(\mathbf{P_L}) = 1 & \text{Vessel surface} \\ \mathcal{L}(\mathbf{P_L}) > 1 & \text{Vessel exterior} \\ \mathcal{L}(\mathbf{P_L}) < 2 & \text{Graph neighbourhood interior} \\ \mathcal{L}(\mathbf{P_L}) = 2 & \text{Graph neighbourhood boundary} \\ \mathcal{L}(\mathbf{P_L}) > 2 & \text{Graph neighbourhood exterior} \end{cases} \tag{A.3}$$

Anatomically some vessel segments may physically touch or nearly touch an adjacent vessel. Furthermore some vessels are highly curved such that they appear kinked, causing vessel walls to touch or nearly touch. These circumstances cause vessel features to be joined or merged in a non-physical manner in derived isosurfaces. To avoid these artefacts the level set image was altered using gradients of external medial axis images. During level set image computation the nearest graph point indices for each voxel are also stored and were used to create a vessel segment label image, i.e. an image where the intensity defines the label number of the nearest vessel segment. The magnitude of the gradient of this image is only non-zero for transition regions where the intensity switches from one label to the next, and is known as the graph's external medial axis. This type of external medial axis aids in correction of segment-to-segment merging.

To correct for self merging another type of external medial axis image is required. For each graph segment a geodesic graph distance from one end point to the next can be computed, which, using the nearest graph point indices for each voxel, can be used to create an image representing local geodesic curve distance. Locations where the magnitude of the gradient of this image is higher than some threshold forms an external medial axis. The threshold used here is 2π times the maximum radius of the segment.

A single combined binary external medial axis image $\mathcal{M}$ was formed by combining the before mentioned, graph labelling derived, external medial axis image, with these individual, graph segment geodesic distance derived, versions. To avoid separations at graph segment branch points, where merging should take place, $\mathcal{M}$ is set to 0 within a distance of π times the radius at a branching point. Finally the level set image $\boldsymbol{\mathcal{L}}(\mathbf{P_L})$ was set to 2 where $\mathcal{M} = 1$.

Figure 3 visualises a vessel segment label image with level set correction regions shown in black. The figure illustrates how regions of potential self merging and potential segment-to-segment merging can be altered.